POLISH MARITIME RESEARCH 2 (126) 2025 Vol. 32; pp. 4-16
10.2478/pomr-2025-0016

Similarity Study of the Turbulence Characteristics of Underwater Vehicle Models

Guozhi Bao[1] *
Bolong Liu[1]
Ruitao Yang[1]
Xiaodong Si[1]
[1] School of Energy and Power, Jiangsu University of Science and Technology, Zhenjiang Jiangsu, China

* Corresponding author: *gzbao2005@163.com (Guozhi Bao)*

ABSTRACT

To achieve dynamic similarity with the experimental characteristics of structural flow, experimental models are often designed to stimulate turbulence that mimics high Reynolds number conditions. However, the size, shape, and placement of the trip wires play a crucial role in effectively exciting turbulence. This paper focuses on the SUBOFF scaling model as the subject of investigation. The RANS method was employed to analyse the flow field characteristics of a rotating body model with different excitation filaments, and the flow field properties of the model under trip wire perturbation were compared with those of a full-scale model at a 1:17.5 scaling ratio, to ensure similarity in terms of the Froude number. The goal was to identify the trip wire installation solution that most closely resembled the flow field characteristics of the full-scale model. The study found that the trip wire altered the boundary layer structure. Different installation positions of the trip wire led to varying effects on the boundary layer and local pressure gradient, which in turn affected the recovery of the boundary layer and modified the local flow field structure. By satisfying the condition for Froude number similarity, an experimental model subjected to surge filament perturbation can accurately simulate a pressure gradient, turbulence intensity, and vortex core structure that are comparable to those of a full-scale model. This finding offers a new approach for experiments focused on achieving high Reynolds number similarity.

Keywords: Froude number, turbulence intensity, boundary layer, trip wire

INTRODUCTION

Experiments have become a crucial method for investigating scientific problems in the engineering sciences and various fields of applied research. In the domain of ship design, testing is not only carried out to assess the quality of the design, but also to analyse and evaluate its theoretical foundation and level of innovation.

Sahoo et al. [1] examined detailed trends and future research directions in autonomous underwater vehicles (AUVs), and provided valuable insights for their future development. Subsequently, Panda et al. [2] offered a comprehensive summary of studies of AUV hydrodynamic characteristics, and discussed the turbulence models used in numerical simulations related to computational fluid dynamics (CFD). Their work is highly significant in terms of experimental techniques and the computational analysis of hydrodynamic parameters. Mitra et al. [3] investigated the hydrodynamic characteristics of AUVs in shallow environments based on the Reynolds stress model; their experimental results provide an approach for the enhancement of AUV design for shallow environments. Following this, Mitra et al. [4] further investigated the hydrodynamic characteristics of AUVs under the influence of a rotating flow field in a shallow environment, in which the effects of different rotational speeds and rotating flow intensities on the drag, skin friction and pressure coefficients of AUVs were analysed to provide a reference for the design of AUVs in shallow environment.

Sun et al., Xiang et al., and Guo et al. [5-7] conducted extensive experiments on the SUBOFF model in a circulating water channel (CWC) equipped with a planar motion mechanism (PMM). Their studies included oblique towing tests, pure yaw tests, and pure sway tests. Despite the advantages of PMM tests, such as their similarity to actual flow fields, minimal boundary effects, and improved measurement accuracy, there are also disadvantages associated with conducting these tests in a towed pool, which include limited measurement duration, motion errors due to track deformation, high levels of vibration interference, and challenges in observation. In contrast, a CWC allows water to flow around the model, enabling prolonged testing periods. Furthermore, the trailer movement in a CWC is smoother, and is not constrained by a longitudinal track.

Researchers have conducted water tunnel tests to evaluate the hydrodynamic performance of AUVs of various sizes, and have yielded accurate results by analysing the forces and moments during steady-state turning in a rotating arm manoeuvre test [10-12]. Chen et al. [13] considered the influence of hydrodynamic derivatives throughout the motion process, and employed the RANS method to assess the hydrodynamic performance of the moving submarine. Their work provided valuable insights for modelling the forces and moments experienced by the submarine during motion, thereby enhancing the accuracy of the tests.

The use of hydrodynamic properties derived from model-scale structures to analyse the performance of full-scale structures has become a common methodology. Moonesun et al. [14] compared CFD simulations with the results of pool tests following model scaling, providing a method for reducing a full-scale submarine model to a model scale that exhibits similar speed and drag during fully submerged underwater tests. The validity of the scaling method was confirmed by comparing the pressure distributions on the surface and at the free surface of the structure between the real and model scales [15].

However, the speeds required for the test model to achieve Reynolds number similarity cannot be attained in towed pool, water tunnel, or wind tunnel tests. According to Froude's law, the speed of a real vessel (such as a ship or submarine) is scaled down for the model during testing; the ratio of the model's speed to that of the full-scale vessel is proportional to the square root of the vessel's length [16-18]. To satisfy the requirement for Froude number similarity, the boundary layer structure around the ship can be modified through external means to achieve real-scale simulations for specific cases. Wang et al., Zhou et al., and Ling et al. [19-21] analysed the hydrodynamic effects of turbulent pulsation pressure resulting from boundary layer separation, transition, and development. Liu et al. [22] investigated the drag and flow field characteristics of the SUBOFF model under various scenarios based on the RANS equations. Verdoya et al. [23] employed proper orthogonal decomposition (POD) to identify the free-flow structures with the highest correlation with the boundary layer structures, and also investigated the effects of parameters such as the Reynolds number and pressure gradient on the free-flow modes and the correlation structures within the boundary layer. Qu et al. [24] used the large eddy simulation (LES) method to study the vortex structures around a rotating body, and examined the development processes of horseshoe vortices, hairpin vortices, and ring vortex structures based on the Q-criterion. Jiménez et al. and Shariati et al. [25] investigated the impact of attachments on the hydrodynamic characteristics of submarines, and concluded that these attachments are a crucial factor influencing hydrodynamic features such as vortex volume and pressure. The arrangement of vortex control baffles around the appendages helps to suppress the generation of horseshoe vortices by creating small-scale vortices in the opposite direction to that of the horseshoe vortex, due to a reverse pressure gradient around the baffles. These small vortices subsequently merge into a larger vortex that interacts with the horseshoe vortex [26]. This study investigates the effect of adding an excitation filament to the SUBOFF model on the flow field, in conjunction with the vortex-shaving effect of the vortex-control baffle. Wang et al. [27] examined the characteristics of the flow field after incorporating a trip wire at the bow and found that the pressure distribution and vortex structure remained unchanged compared to those before the addition of the trip wire. Morse et al. [28] analysed the development of the laminar boundary layer upon encountering a trip wire, as well as the subsequent changes in the turbulent boundary layer. Changing the position of the trip wire altered the boundary layer dynamics and the local pressure gradient, which in turn affected the recovery of the boundary layer after the trip wire, thereby modifying the local flow field structure. Conducting related research can be of great help in the study of underwater communication and positioning of underwater vehicles [32-34]. Although there have been numerous studies of the flow field characteristics of SUBOFF through experiments, there is a notable lack of model-scale simulations examining these flow field characteristics at high Reynolds numbers.

In the present paper, trip wires were installed at both the bow and stern of the SUBOFF model, and the RANS method was employed to analyse the flow field characteristics at both full scale and model scale with the trip wires in place. The study investigated the pressure, turbulence intensity, and vortex structure at various locations on the model with different trip wire configurations, while maintaining a similar Froude number. By comparing the flow field characteristics of the full-scale SUBOFF model at corresponding positions, the aim was to identify the trip wire mounting configuration on the test model that most closely resembled the flow field of the full-scale SUBOFF model.

NUMERICAL METHOD AND MODEL

GOVERNING EQUATIONS

In this paper, the instantaneous values in the equations are replaced with average and fluctuation values, and are solved using the Reynolds-averaged Navier-Stokes (RANS) approach. When addressing practical engineering problems, we focus on the time-averaged value of each turbulence cell, which requires a relatively small number of grid cells and a low computation time. In addition, the results obtained in this study meet the requirements of practical engineering applications. The RANS method is based on variable decomposition, in which instantaneous physical quantities are separated into time-averaged and fluctuating components. The governing equation for an incompressible Newtonian fluid, derived from the RANS equations, is expressed as follows:

$$\frac{\partial U_i}{\partial x_i} = 0 \tag{1}$$

$$\frac{\partial U_i}{\partial t} + U_j \frac{\partial U_i}{\partial x_j} = -\frac{1}{\rho}\frac{\partial P}{\partial x_i} + \frac{\partial}{\partial x_j}\left[\nu\left(\frac{\partial U_i}{\partial x_j} + \frac{\partial U_j}{\partial x_i}\right)\right] - \frac{\partial \overline{u_i^{'}u_j^{'}}}{\partial x_j} + f_i \tag{2}$$

where U_i represents the average speed, $u_i^{'}$ is the pulsation speed, $\overline{u_i^{'}u_j^{'}}$ is the Reynolds stress term, x_j is the direction of the coordinate axis, f_i is the mass force, ν is the kinematic viscosity of the fluid, ρ is the density of the fluid, and t is time.

To convert Eq. (2) into a closed-form equation, a turbulence model is used. We apply the realisable k-epsilon model, due to its high numerical stability and accuracy in solving the pressure gradient. The equations for the dissipation rate and turbulent energy transport are as follows:

$$\rho\frac{d\varepsilon}{dt} = \frac{\partial}{\partial x_j}\left[\left(\mu + \frac{\mu_t}{\sigma_\varepsilon}\right)\frac{\partial \varepsilon}{\partial x_j}\right] + \rho C_1 S\varepsilon - \rho C_2\frac{\varepsilon^2}{k + \sqrt{\nu\varepsilon}} + C_{1\varepsilon}\frac{\varepsilon}{k}C_{3\varepsilon}G_b \tag{3}$$

$$\rho\frac{dk}{dt} = \frac{\partial}{\partial x_j}\left[\left(\mu + \frac{\mu_t}{\sigma_k}\right)\frac{\partial k}{\partial x_j}\right] + G_k + G_b - \rho\varepsilon - Y_M \tag{4}$$

where G_b represents the turbulent kinetic energy generated by buoyancy, G_k denotes the turbulent kinetic energy generated by the average velocity gradient, Y_M represents the influence of turbulent pulsation expansion on the total dissipation rate, μ is the dynamic viscosity caused by diffusion, μ_t is the turbulent viscosity coefficient, ε is the dissipation rate, S is the average strain rate, k is the turbulent kinetic energy, $C_1 = \max\left[0.43, \eta/(\eta+5)\right]$, $\eta = S \cdot k \cdot j \cdot \varepsilon$ is a symbol, C_2 and $C_{1\varepsilon}$ are constants, $C_{3\varepsilon}$ is a function representing the effect of buoyancy on the dissipation rate, and σ_ε and σ_k are the turbulent Prandtl numbers of the dissipation rate ε and the kinetic energy k, respectively.

According to Froude's similarity criterion, to ensure the similarity of two flow systems influenced by gravity, the ratio of the inertial forces in the fluid must be equal to the ratio of the gravitational forces. The ratio of the velocities of the model and the real-scale ship is also proportional to the square of the ratio of the characteristic lengths of the model and the real-scale ship, as dictated by the Froude similarity criterion. Based on the scaling ratio between the real-scale ship and the model, we can derive the relationship between the model speed and the real-scale ship speed. The mathematical expression for the Froude number is given below:

$$F_r^2 = \frac{U^2}{gL} \tag{5}$$

where U is the speed, L is the captain, and g is the acceleration of gravity.

NUMERICAL MODEL

The real-scale underwater rotary body uses the SUBOFF profile, and its scaling parameters are presented in Table 1.

Table 4 presents a comparison between the calculated drag values and the experimental data [8] for the four domains at a speed of 10 knots. To prevent data reflux, velocity inlet and pressure outlet boundary conditions are applied across all computational domains. The errors in the calculated values for domains C and D are the smallest, and remain constant. To facilitate a more detailed analysis of the hydrodynamic characteristics of the wake field, domain C is selected for the subsequent calculations [25].

Fig. 1 illustrates the dimensions and boundary condition settings of the computational domain. The dimensions of the computational domain are 12L × 4L × 4L, with the head end of the SUBOFF model positioned 3L from the inlet and the tail end 8L from the outlet. The location of the trip wire is depicted in Fig. 2. To achieve more accurate flow field characteristics, grid refinement was applied near the trip wire, attachments, and hull.

In our calculations, the value of y^+ was set to 60, and the boundary layer was defined with eight layers, with a growth rate of 1.2 [9]. The grid near the wall is illustrated in Fig. 3. The pressure-velocity coupled iterative solution was obtained using the SIMPLE algorithm, with the pressure terms presented in standard discrete format, and the momentum, turbulent kinetic energy, and turbulent dissipation rate were calculated using a second-order upwind scheme.

Tab. 1. Geometric parameters of the full-scale SUBOFF model

Parameter	Unit	Value
Total length	m	76.23
Head minister	m	17.78
Parallel middle body length	m	39.0075
Stern minister	m	19.4425
Maximum radius in the middle	m	4.445
Command room enclosure height	m	3.605
Maximum thickness	m	1.155

Tab. 2. Geometric parameters of the DARPA SUBOFF model

Parameter	Unit	Value
Total length (*L*)	m	4.356
Head minister	m	1.016
Parallel middle body length	m	2.229
Stern minister	m	1.111
Maximum radius in the middle (R_{max})	m	0.254

Tab. 3. Trip wire installation configurations

Program	Placement	Size (height/mm)	Size (width/mm)
1	*x*/*L*=0.20	10	20
	x/*L*=0.75	15	10
2	*x*/*L*=0.20	10	20
	x/*L*=0.75	20	10
3	*x*/*L*=0.20	10	20
	x/*L*=0.75	25	10
4	*x*/*L*=0.20	15	20
	x/*L*=0.75	18	10
5	*x*/*L*=0.20	15	20
	x/*L*=0.75	20	10
6	*x*/*L*=0.20	18	20
	x/*L*=0.75	18	10
7	*x*/*L*=0.20	18	20
	x/*L*=0.75	20	10
8	*x*/*L*=0.20	18	20
	x/*L*=0.75	25	10
9	*x*/*L*=0.20	20	20
	x/*L*=0.75	25	10

Tab. 4 Independence tests of the computational domain at 10 knots

Domain	Size (width × height × length)	**Fd**/N	
		CFD	Experiment [8]
A	*2L×2L×4L*	293	283.8
B	*3L×3L×8L*	290	283.8
C	*4L×4L×12L*	287	283.8
D	5L×5L×13L	287	283.8

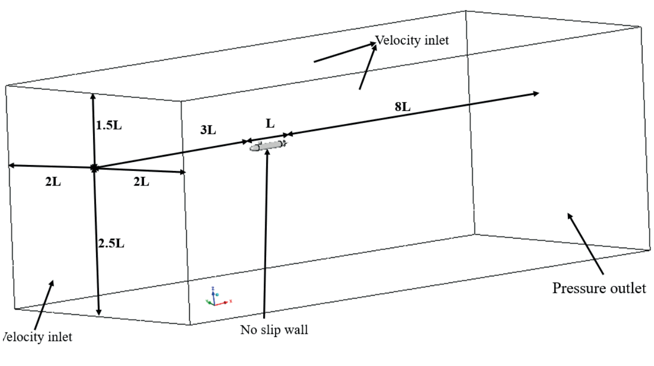

Fig. 1. Computational domain for simulation of the DARPA SUBOFF model

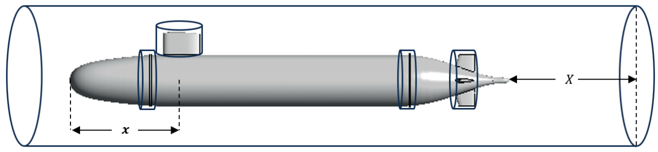

Fig. 2. Grid encryption area for the DARPA SUBOFF model

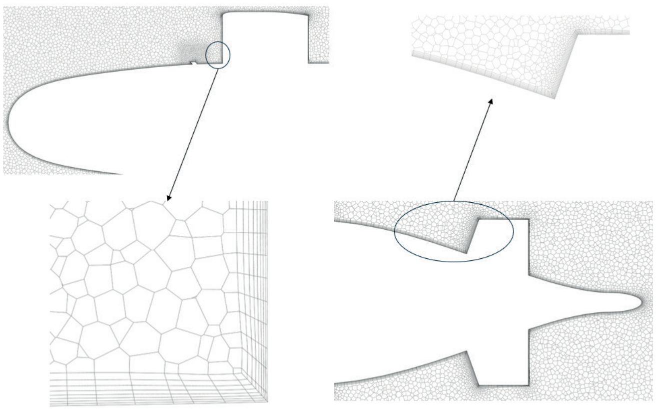

Fig. 3. Near-wall mesh for the DARPA SUBOFF model

IRRELEVANCE TEST

To verify the accuracy of the numerical simulation, calculations were performed using the same numerical simulation method and the results were compared with experimental measurements. In the numerical verification calculations, the SUBOFF model was not equipped with a trip wire [29]. The drag coefficients (C_d) from the experimental and simulated data were calculated as follows:

$$C_d = \frac{2F_d}{\rho v^2 A} \tag{6}$$

where F_d is the value of the resistance for the SUBOFF model, v is the speed, and A is the wet surface area.

Table 5 presents a comparison between the CFD and experimental drag values for the full attachment model at five different speeds. It can be seen that the average error for three of these speeds is 1.33%, with a maximum error of 2.26% between the CFD and experimental values, a value which meets engineering standards. To further verify the accuracy of the numerical calculations, the pressure coefficient (C_P) at the upper half edge of the mid-longitudinal plane and at half the height of the sail was compared at a speed of 10 knots.

$$C_P = \frac{2P}{\rho v^2} \tag{7}$$

where P is the surface pressure, ρ represents the density of the fluid, and v is the speed.

The distribution of pressure coefficients along the centre longitudinal plane and at the midpoint of the sail is shown in Fig. 4. It is evident that the pressure coefficient distributions at these two locations are closely aligned with the experimental data. The pressure coefficients are higher at the bow, the front of the sail, and the leading edge of the fin, due to the head-on flow and lower fluid velocities at these three points.

Tab. 5. Analysis of drag results at five different speeds

Velocity/kn	Experiment [8]		CFD		Error
	F_d/N	C_d	F_d/N	C_d	
6	102.3	0.003464	103	0.003487	0.68%
10.00	283.8	0.003384	287	0.003419	1.05%
16.00	675.7	0.003147	691	0.003218	2.26%

installed at (x/L = 0.20) and (x/L = 0.75) to alter the boundary layer structure. Subsequently, the velocity distribution, pressure distribution, turbulence intensity, and vortex structure were observed at different profiles.

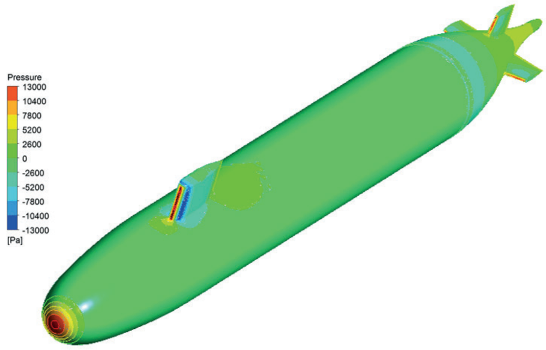

Fig. 5. Pressure clouds on the surface of the SUBOFF model at 10 knots

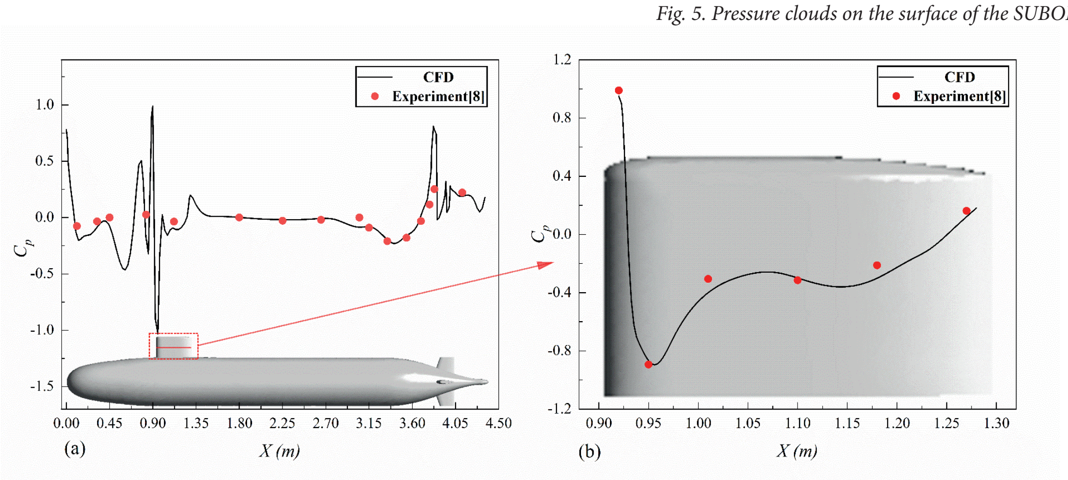

Fig. 4. Distribution of pressure coefficients along the centre longitudinal plane and at the midpoint of the sail

RESULTS AND DISCUSSION

There are nine options for the placement of the trip wire, as shown in Table 3, where x/L represents the ratio of various hull positions to the length of the boat, indicating the trip wire's location and the selected profile. Figs. 5 and 6 illustrate the pressure distribution on the hull surface and the velocity distribution along the centre longitudinal plane at a speed of 10 knots. It can be observed that the maximum pressure on the surface occurs at the front of the bow, the sail, and the fin, where the pressure increases due to the decrease in velocity caused by the head-on flow. Following this, the increase in flow velocity leads to the formation of a low-pressure area behind the high-pressure zone. The pressure gradient in the midbody section is small. At the junction between the midbody and the transom, the sudden reduction in the hull's diameter results in a rapid increase in speed and a corresponding drop in pressure, creating a low-pressure zone. Based on the numerical distributions of pressure and velocity fields, a trip wire was

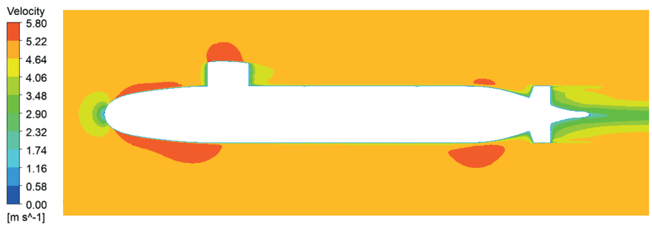

Fig. 6. Velocity cloud on the centre longitudinal plane at 10 knots

FLOW FIELD ANALYSIS

The drag velocity of the model is difficult to achieve when a high similarity in the Reynolds number is required for water tunnel experiments [14]. To facilitate a more accurate analysis of the real-scale motion characteristics at the model scale, experiments were conducted by scaling the speed of the actual ship to the model according to Froude's law. The analysis focused on the effects of different (x/L) values on the velocity distribution after installing the trip wire on the model.

Fig. 7 illustrates the radial velocity distribution for the full-scale model at various positions along the hull and the stern of the boat while traveling at 20 knots. When compared with the velocity distribution observed in the centre-longitudinal plane, it is evident that the flow in the forebody of the submarine is influenced by the stagnation zone and the pressure gradient along the forebody. The boundary layer in this region is relatively thin, but thickens as it passes over the forebody, becoming turbulent under the influence of the sail. This turbulence contributes to the formation of a complex and unstable wake behind the sail. Fig. 7(c) reveals that the flow field at the surface of the paddle disc takes on a cloverleaf shape due to the influence of the fin. In addition, a V-shaped region is formed above the cloverleaf as a result of the horseshoe vortex generated behind the sail. Unstable vortices at the tip of the fin and at the junction between the fin and the hull impact the boundary layer, leading to the creation of a complex wake field behind the boat. To enable further analysis, Fig. 8 illustrates the distribution of radial pressure gradients at different cross-sections at a sailing speed of 20 knots. Due to the decrease in velocity and the increase in pressure caused by the head-on flow on the surface of the sail, as shown in Figs. 7(a) and 8(a), a high-pressure region forms at the front of the sail. Following this, the flow velocity increases at the back of the sail, creating a low-pressure region, as illustrated in Figs. 8(a) and (b). The pressure in the wake field is distributed circularly, with the pressure gradient decreasing as the flow develops in all directions. This behaviour is similar to the turbulence development in the flow field behind the boat, where the turbulent region in the wake exhibits a circular distribution, expanding outward in all directions as the flow progresses and the turbulence intensity diminishes.

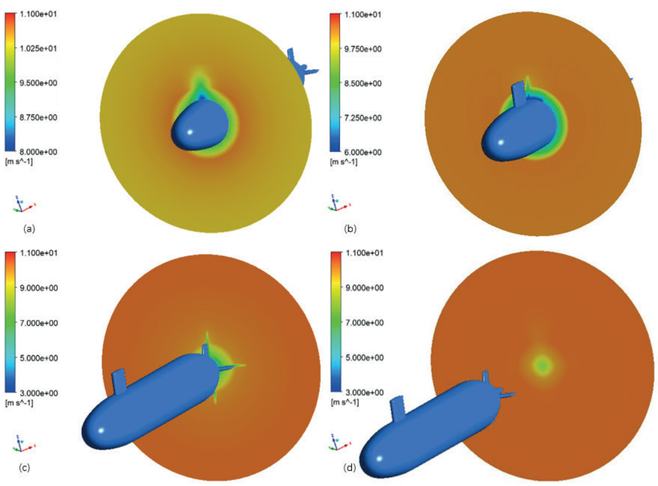

Fig. 7. Distribution of radial velocity at different positions for the full-scale model at 20 knots:
(a) x/L = 0.2 (b) x/L = 0.32 (c) x/L = 0.978 (d) x/L = 1.31.

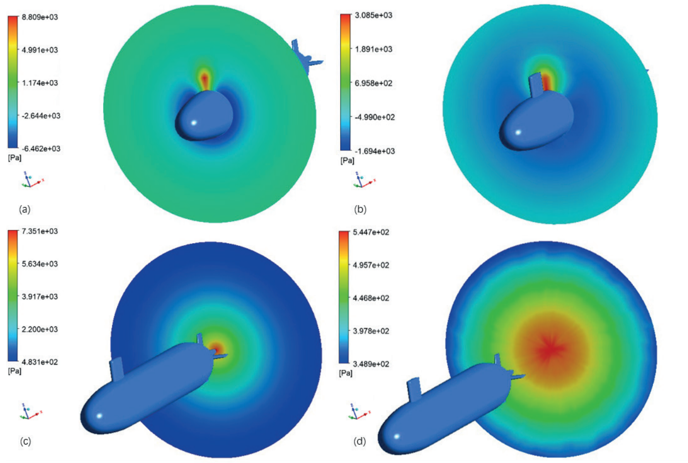

Fig. 8. Distribution of radial pressure gradient at different positions at 20 knots for full-scale submarine:
x/L = 0.2 (b) x/L = 0.32 (c) x/L = 1.01 (d) x/L = 1.31.

Figs. 9 and 10 illustrate the distributions of radial velocity and pressure gradient at the front and back of the sail for a model-scale submarine operating at 5 knots, under different trip wire installation configurations. The boundary layer is modified by the trip wire, which influences the local flow field around the sail. The flow field distributions shown in Figs. 9(a) and 10(a) at x/L=0.2 indicate that the pressure gradient decreases and spreads slightly in the radial direction as the height of the trip wire increases. The effect of the trip wire on the flow field behind the sail results in a reduction in the velocity near the submarine compared to the full scale, while the trend in the velocity distribution in the radial direction remains similar to that of the actual scale. This observation is consistent with the results presented in Figs. 9(b) and 10(b). As the height of the trip wire increases, the pressure distribution spreads and increases in all directions. This aligns with the understanding that the trip wire can significantly affect turbulence and pressure gradients [27, 28]. Based on the scaling ratio between the real scale and the model scale, the velocity distribution and pressure distribution in the radial direction at the bow of the model closely resemble the real scale flow field when the similarity of the Froude number is satisfied in Cases 1, 2, and 3.

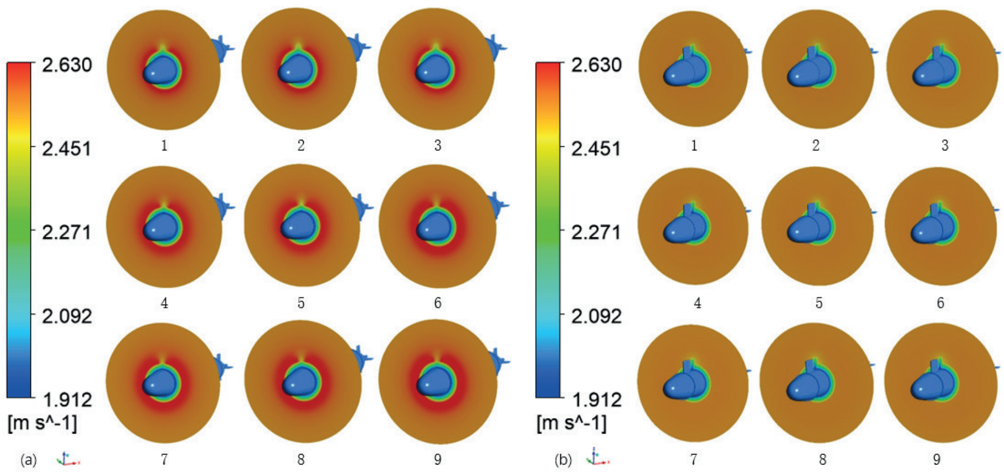

Fig. 9. Radial velocity distribution of the underwater rotary at 5 knots in different cases:
(a) x/L = 0.2 (b) x/L = 0.32

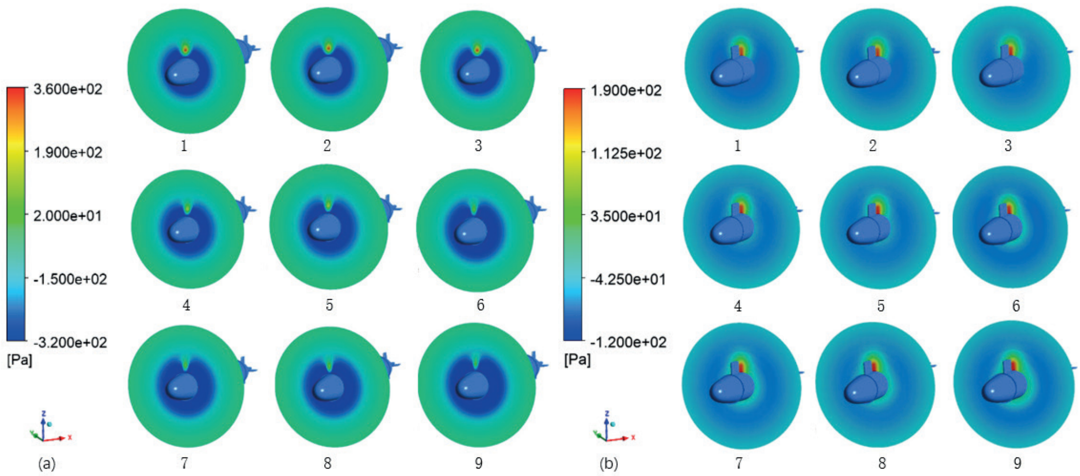

Fig. 10. Radial pressure gradient distribution of the underwater rotary at 5 knots in different cases:
(a) x/L = 0.2 (b) x/L = 0.32

Figs. 11 and 12 show the distributions of radial velocity and pressure gradient on the paddle surface and in the wake flow field at 5 knots, corresponding to different trip wire installation configurations at the model scale. As can be seen from Fig. 11(a), the radial velocity distribution at the paddle surface for Case 1 forms a four-leaf clover pattern. The presence of the trip wire slightly decreases the velocity near the hull. In the other cases, as the height of the trip wire increases, the four-leaf clover pattern transitions to a circular distribution, while a V-shaped region formed by the horseshoe vortex appears across all cases.

By comparing the radial velocity distributions at *x/L* = 1.31 in Figs. 7(d) and 11(b) at the real scale and the model scale, it is evident that the model scale, particularly in Case 1, most closely resembles the distribution observed at the real scale, in accordance with the Froude number similarity criterion. In both figures, the values range from small to large in a circular pattern emanating from the centre, creating a striped area directly behind the sail. While the tendency for velocity to increase from the inside to the outside is somewhat mitigated by the influence of the surge filaments, the overall structure of the radial velocity distribution remains consistent.

Fig. 12 illustrates the pressure distribution in the radial direction at *x/L* = 1.01 and 1.31. At *x/L* = 1.01, the pressure gradient decreases with increasing trip wire height, whereas at *x/L*=1.31, it increases. This behaviour is aligned with the observed velocity distribution in the radial direction. When comparing the real-scale pressure distribution, it is evident that the pressure gradient increases under the trip wire condition, as the trip wire alters the boundary layer structure and affects the wake flow field. An analysis of the velocity and pressure distributions at the paddle surface and the wake flow field, and a comparison of the numerical distributions of radial velocity and pressure gradients at the real scale with those from multiple profiles for each case based on Froude number similarity, indicate that the characteristics of the flow field in Case 1 are the most analogous to those of the real-scale flow field.

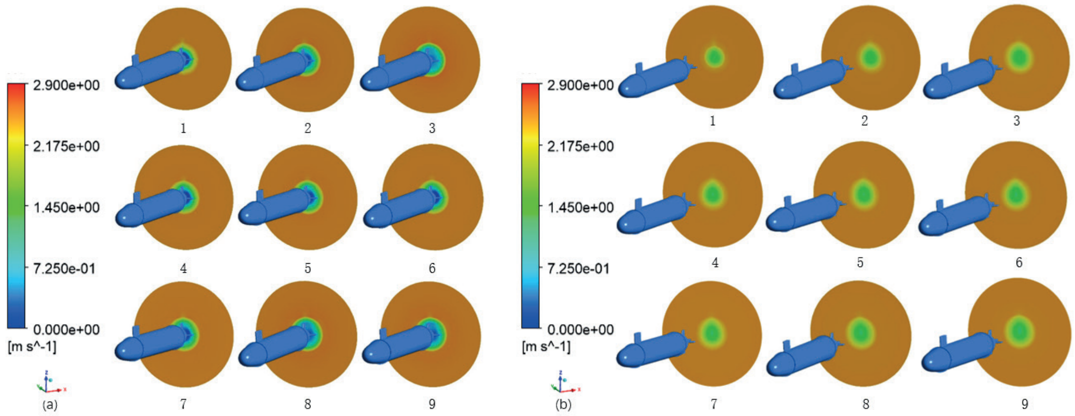

Fig. 11. Radial velocity distribution for the underwater rotary scenario at 5 knots in different cases:
(a) x/L = 0.978 (b) x/L = 1.31

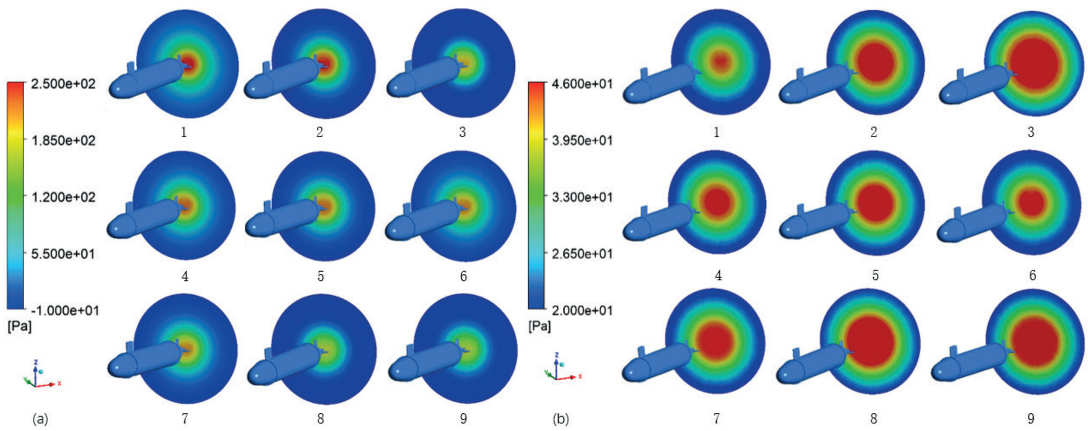

Fig. 12. Radial pressure gradient distribution for the underwater rotary scenario at 5 knots for different cases:
(a) x/L = 1.01 (b) x/L = 1.31

Fig. 13 illustrates the distribution of $\overline{U}/U_\infty$ in the radial direction for both the real scale and each working condition. The turbulence intensity distribution in the absence of trip wire is consistent with the numerical simulation results reported by Zhao et al. [31]. Here, represents the mean streamwise velocity, while denotes the free stream velocity. From Figs. 13(a) and (b), it is evident that the interaction between the front end of the sail and the trip wire results in an increase in velocity, with the change in velocity becoming more pronounced as the diameter of the trip wire increases. The velocity distribution above the sail has a minimal impact on the overall velocity distribution, and the velocity distribution in the radial direction behind the sail is less influenced by the trip wire. Due to the effects of the tip vortex and horseshoe vortex, the velocities at the bottom and top of the sail exhibit a cliff-like distribution, which is aligned with the velocity cloud maps in Fig. 8. Fig. 13(c) shows the velocity distribution in the radial direction at the surface of the paddle disc. Under the influence of the trip wire, the velocity near the hull decreases, and this decrease becomes more pronounced as the diameter of the trip wire increases, resulting in an unstable vortex system. Although the rate of velocity reduction in the radial direction behind the boat decreases, the overall velocity still declines with an increasing trip wire diameter, as illustrated in Fig. 13(d).

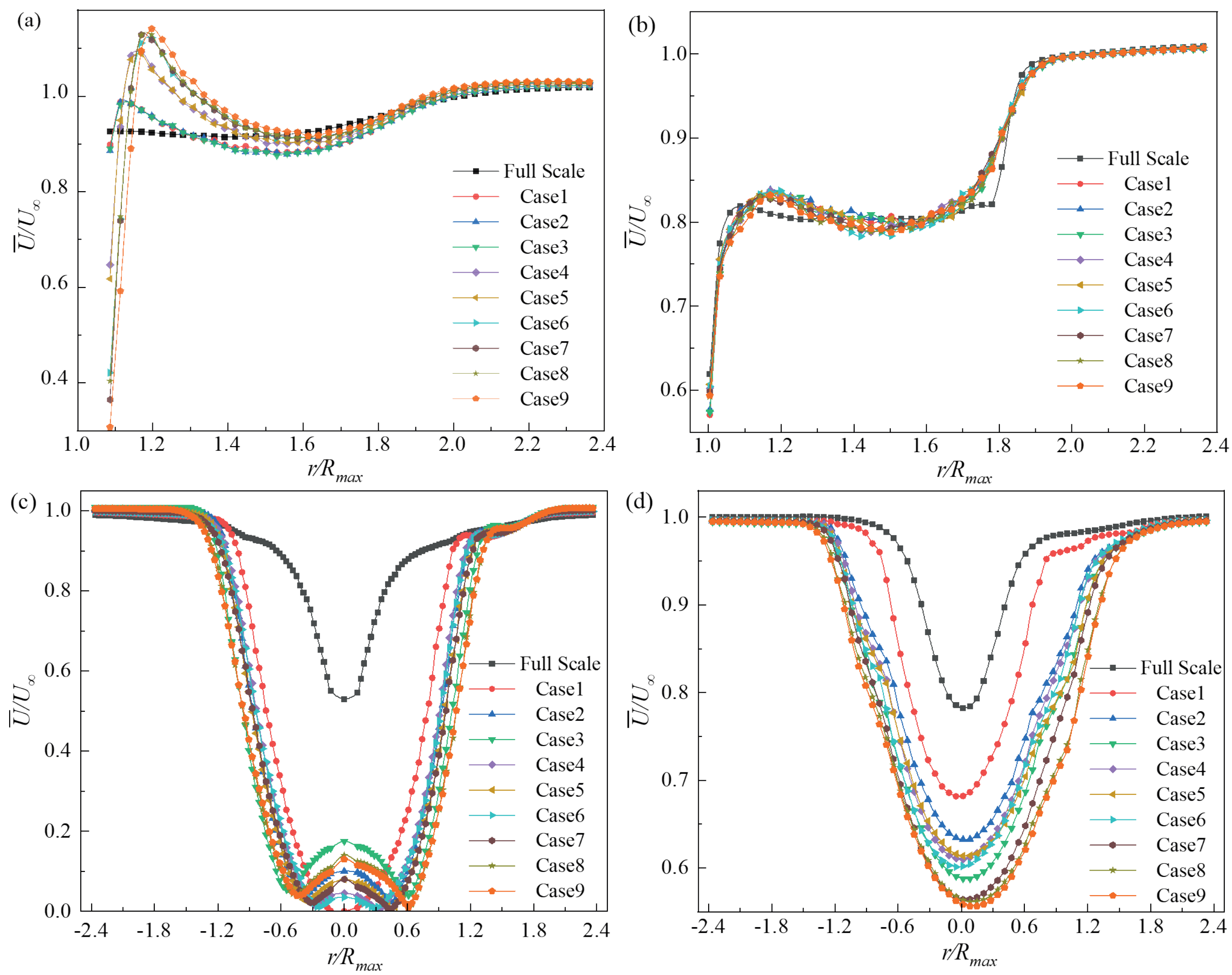

Fig. 13. Distribution of $\overline{U}/U_\infty$ in the radial direction at different cross sections: (a) x/L = 0.2 (b) x/L = 0.32 (c) x/L = 0.978 (d) x/L = 1.31

The distribution of pressure coefficients in the radial direction at the real scale and under various operating conditions is illustrated in Fig. 14. The turbulence intensity distribution in the absence of the trip wire is consistent with the numerical simulation of Zhao et al. [31]. As shown in Figs. 14(a) and (b), the pressure coefficient at the front end of the sail exhibits an initial increase followed by a decrease, with this behaviour becoming more pronounced as the diameter of the trip wire increases. In contrast, the pressure coefficient distribution in the radial direction behind the sail is relatively stable. The pressure coefficient distributions at these two locations correspond to the velocity distributions observed.

Figs. 14(c) and (d) show the pressure coefficient distribution at (x/L = 1.01) and (x/L = 1.31), respectively. At (x/L = 1.01), the pressure coefficient in the radial direction at real scale is higher than under all other conditions, and it decreases with an increase in the diameter of the trip wire. Conversely, at (x/L = 1.31), the pressure coefficient in the radial direction at real scale is lower than under all other conditions, and it increases with the diameter of the trip wire.

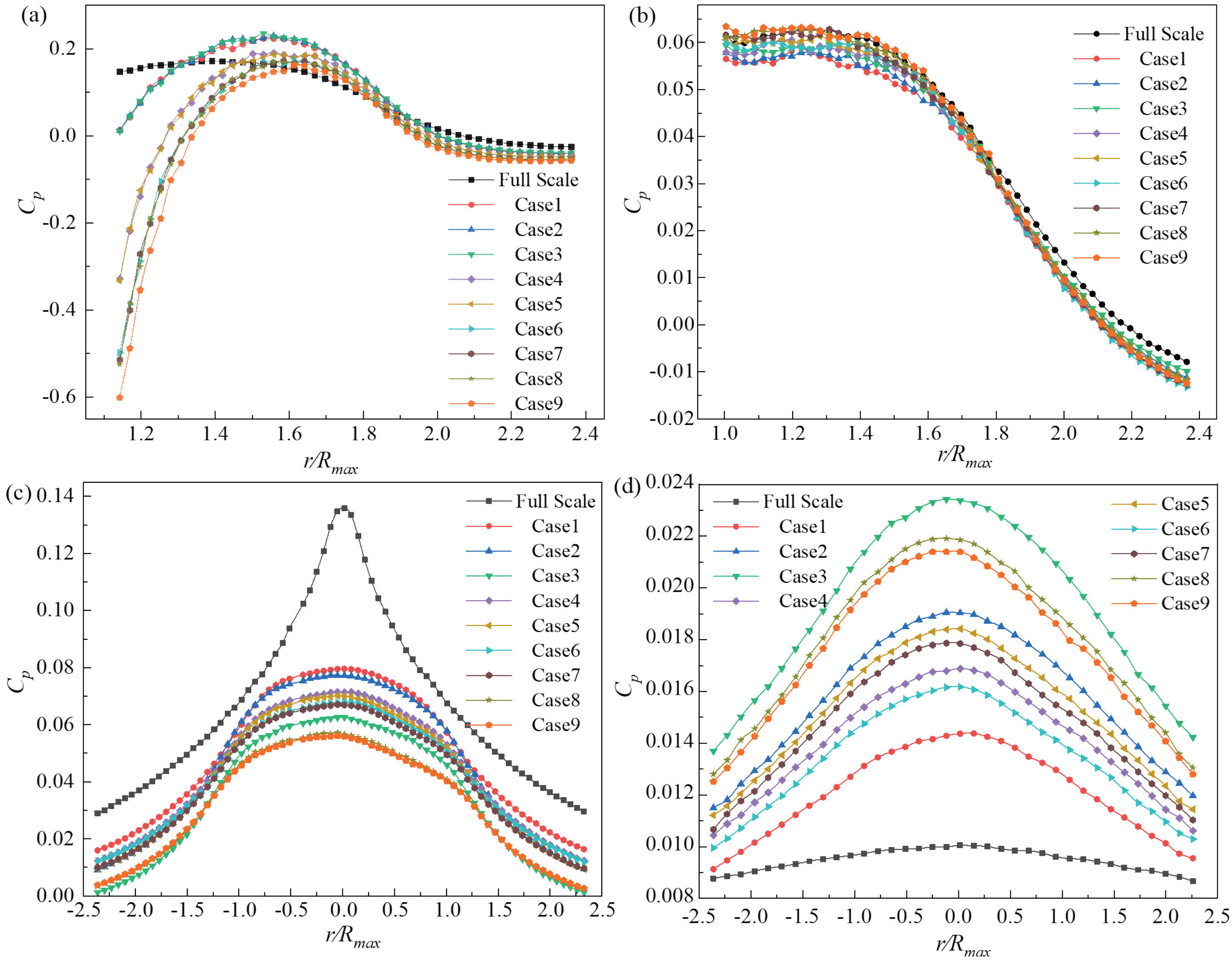

Fig. 14. Distribution of pressure coefficients in the radial direction at different cross sections: (a) x/L = 0.2 (b) x/L = 0.32 (c) x/L = 1.01 (d) x/L = 1.31

TURBULENCE AT VARIOUS PROFILES

The variation in the turbulence intensity along a straight centreline at ($Y = 0$) and ($Z = 0$) behind the boat is illustrated in Fig. 15. This figure depicts how the turbulence intensity changes along the centreline from the stern of the boat to a distance equal to twice its length. As the flow develops, the turbulence intensity at the centre decreases sharply from the stern to one boat length, followed by a more gradual decrease from one to two boat lengths. The turbulence intensity distribution without a trip wire is closely aligned with the experimental data [30, 31]. A comparison of the turbulence intensity variations at the centre of the boat across different operating conditions reveals that the turbulence intensity behind the boat is primarily influenced by the trip wire in the wake. From the stern to one boat length, the turbulence intensity increases in correlation with the diameter of the trip wire. However, from one to two boat lengths, the turbulence intensity across all conditions becomes relatively uniform, and shows less sensitivity to the diameter of the trip wire. Overall, a comparative analysis of the changes in turbulence intensity behind the boat indicates that the trip wire can enhance the turbulence intensity, effectively simulating the flow field state associated with a high Reynolds number.

Fig. 16 illustrates the distribution of turbulence intensity in the radial direction at $X/L = 1$, located behind the boat. The figure shows that turbulence intensity first increases and then decreases in the radial direction. In addition, the rate of decrease in the turbulence intensity becomes less pronounced as the diameter of the trip wire increases. The disturbance caused by the trip wire increases the turbulence intensity. As the fluid flows past the trip wire, it generates a separation bubble downstream, causing the flow to turn at the rear of the bubble and altering the boundary layer structure. By comparing the changes in turbulence intensity in both the axial and radial directions under different conditions, it can be observed that increasing the diameter of the trip wire enhances the influence area of the separation bubbles, resulting in a further increase in turbulence intensity.

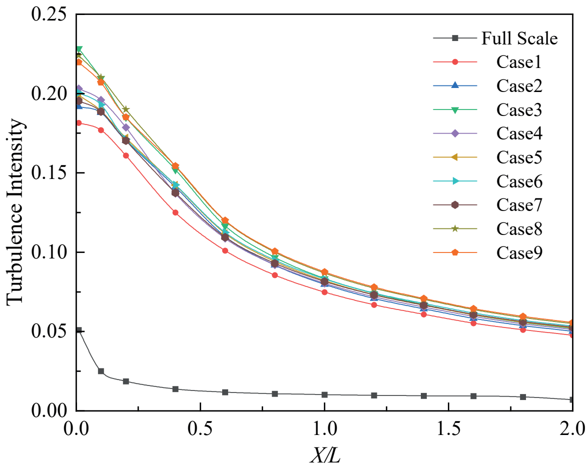

Fig. 15. Variation in turbulence intensity along the Y=0, Z=0 straight centreline after the SUBOFF model in different cases

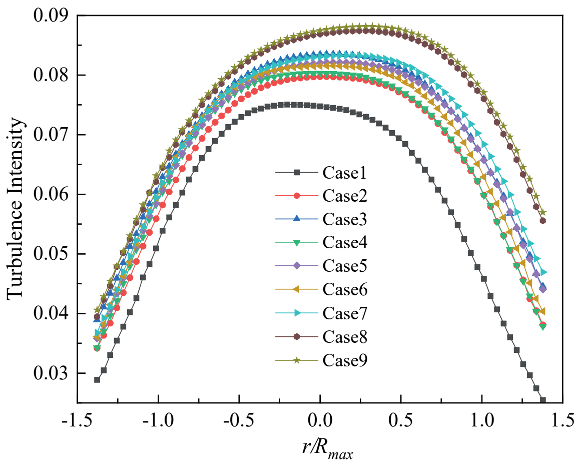

Fig. 16. Distribution of turbulence intensity in the radial direction at the position after the SUBOFF model in different cases

VORTEX STRUCTURE ANALYSIS

Fig. 17 shows the distribution of the vortex core structures in the hull and the surrounding flow field of the real-scale model at 20 knots, as extracted using the Q-criterion. The figure reveals that the parallel mid-body section is largely free of vortex nuclei, with these vortices primarily generated near the sail and the stern. Notably, a distinct wrap-around vortex band forms behind the top of the sail and continues to develop downstream. As the boundary layer on the hull's surface interacts with the sail during flow, a converging flow phenomenon occurs, resulting in the formation of a horseshoe vortex at the interface between the sail and the hull. Fig. 18 compares the distribution of the vortex core structures between Case 1 (with trip wire) and the real-scale model, based on the velocity and pressure gradient distributions for each case. A separation bubble is generated when the boundary layer flows over the trip wire. The instability of the separating bubbles induces turning of the boundary layer, resulting in a complex, multi-scale, non-stationary vortex system. The horseshoe vortex generated by the interaction of the front-end trip wire with the command deck is intensified. In addition, the boundary layer disturbances caused by the aft-end trip wire generate separation bubbles downstream of the wake, leading to increased turbulence. The implementation of an equal scaling model to simulate the characteristics of high Reynolds number flow fields provides valuable insights for the experimental validation of high Reynolds number pools aimed at vortex clipping and turbulence intensity reduction.

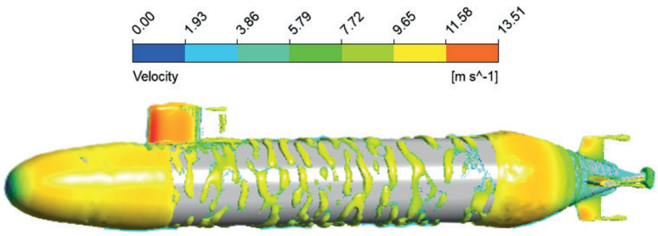

Fig. 17. Distribution of the vortex kernel structure in a full-scale model at 20 knots

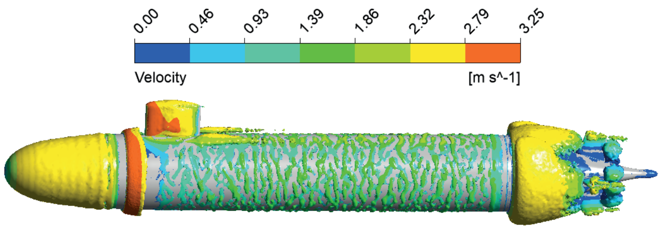

Fig. 18. Distribution of the vortex core structure at 5 knots (Case 1)

CONCLUSION

In order to verify the experimental effects at high Reynolds numbers in water tunnel experiments, we compared the radial velocity and pressure gradient distributions at various locations on the 1:17.5 scaled model with those of the full-scale model under the influence of disturbance from the trip wire. From an examination of the changes in turbulence intensity resulting from different trip wire installation methods and an analysis of the distribution of the vortex core structure within the hull and the surrounding flow field, we can draw the following conclusions:

1) As the size of the surge filament increased, the radial velocity and pressure gradient distributions spread out from the centre in all directions. A comparison of the distribution trends for each case with the full-scale model revealed that Case 1 had the most similar radial velocity and pressure gradient distribution to the full scale.

2) The change in turbulence intensity along the axial centreline at $Y = 0$, $Z = 0$, and in the radial direction at the $X/L = 1$ position behind the boat was analysed for each trip wire condition. The turbulence intensity significantly increased under the disturbance from the trip wire and rose with the size of the trip wire.
3) A separating bubble was generated by the trip wire perturbation, which subsequently developed into a non-constant vortex system. A comparison of the distribution of the real-scale vortex core structure at 20 knots indicates that the horseshoe vortex and tip vortex regions are slightly enlarged. This observation is valuable in regard to the experimental validation of high Reynolds number conditions for vortex clipping and turbulence intensity reduction.

ACKNOWLEDGEMENTS

This work was financially supported by Innovation and Entrepreneurship Program of Jiangsu Province (No. JSSCBS20210994), The Natural Science Foundation of the Jiangsu Higher Education Institutions of China (No. 23KJB430015), Postgraduate Research & Practice Innovation Program of Jiangsu Province (KYCX25_4402), and the China Postdoctoral Science Foundation (No. 2023M732564).

REFERENCES

1. Sahoo A, Dwivedy SK, Robi PS. Advancements in the field of autonomous underwater vehicle. Ocean Engineering 2019, 181, 145-160. https://doi.org/10.1016/j.oceaneng.2019.04.011

2. Panda JP, Mitra A, Warrior HV. A review on the hydrodynamic characteristics of autonomous underwater vehicles. Proceedings of the Institution of Mechanical Engineers, Part M: Journal of Engineering for the Maritime Environment 2020, 235, 15-29. https://doi.org/10.1177/1475090220936896

3. Mitra A, Panda JP, Warrior HV. Experimental and numerical investigation of the hydrodynamic characteristics of autonomous underwater vehicles over sea-beds with complex topography. Ocean Engineering 2020, 198, 106978. https://doi.org/10.1016/j.oceaneng.2020.106978

4. Mitra A, Panda JP, Warrior HV. The hydrodynamic characteristics of autonomous underwater vehicles in rotating flow fields. Proceedings of the Institution of Mechanical Engineers, Part M: Journal of Engineering for the Maritime Environment 2024, 238(3), 691-703. https://doi.org/10.1177/14750902231181843

5. Sun H, Hong Y, Yu C. The comparative research on the VPMM experiment and numerical simulation of the SUBOFF model. Journal of Physics: Conference Series. IOP Publishing 2024, 2756(1). https://doi.org/10.1088/1742-6596/2756/1/012055

6. Xiang G, Ou Y, Chen J. A study on the influence of unsteady forces on the roll characteristics of a submarine during free ascent from great depth. Journal of Marine Science and Engineering 2024, 12(5), 757. https://doi.org/10.3390/jmse12050757

7. Guo R, Zan Y, Luo X. Evaluation of hydrodynamic coefficients and sensitivity analysis of a work-class remotely operated vehicle using planar motion mechanism tests. Ocean Engineering 2024, 312, 119037. https://doi.org/10.1016/j.oceaneng.2024.119037

8. Liu HL, Huang TT. Summary of DARPA SUBOFF experimental program data. 1998.

9. Mitra A, Panda JP, Warrior HV. The effects of free stream turbulence on the hydrodynamic characteristics of an AUV hull form. Ocean Engineering 2019, 174, 148-158. https://doi.org/10.1016/j.oceaneng.2019.01.039

10. Cao J, Feng Y, Li Y, Li H, Han C, Sun Y, Liu Z. Research on the hydrodynamic performance of AUVs in small size open channel area. Ocean Engineering 2023, 288, 116190. https://doi.org/10.1016/j.oceaneng.2023.116190

11. Zhao B, Yun Y, Hu F, Sun J, Wu D, Huang B. Hydrodynamic coefficients of the DARPA SUBOFF AFF-8 in rotating arm maneuver: Part I: Test technology and validation. Ocean Engineering 2022, 266, 113148. https://doi.org/10.1016/j.oceaneng.2022.113148

12. Zhang C, Xu Q, Yang H, Peng Z, Li J, Zhou J. Experimental study and numerical simulation of radiated noise from unmanned underwater vehicle. Polish Maritime Research 2024, 31, 131-141. https://doi.org/10.2478/pomr-2024-0057

13. Chen, X, Yao, J. RANS analysis of manoeuvring hydrodynamic performance for a submarine in six degree of freedom motion. Ocean Engineering 2024, 294, 116781. https://doi.org/10.1016/j.oceaneng.2024.116781

14. Moonesun M, Mikhailovich KY, Tahvildarzade D, Javadi M. Practical scaling method for underwater hydrodynamic model test of submarine. Journal of Advanced Marine Engineering and Technology 2014, 38(10), 1217-1224. https://doi.org/10.5916/jkosme.2014.38.10.1217

15. Cui H, Kong Y, Wang X, Yuan Y. Numerical study on scale effect of full-scale submarine sailing near free surface in stratified fluid. In ISOPE International Ocean and Polar Engineering Conference (pp. ISOPE-I). ISOPE 2024.

16. Jackson HA. Submarine design notes. Massachusetts Institute of Technology; 1982, p. 520.

17. Ostrowski Z, Salamon R, Kochańska I, Marszal J. Underwater navigation system based on Doppler shift–measurements and error estimations. Polish Maritime Research 2020, 27(1), 180-187. https://doi.org/10.2478/pomr-2020-0019

18. Xie X, Liu F, Jin G, Liu J, Xu C, Peng Z. Research on the modified echo highlight model for underwater vehicles with combined structures. Polish Maritime Research 2023, 30(3), 163-173. https://doi.org/10.2478/pomr-2023-0049

19. Wang Y, Gao Y, Liu C. Galilean invariance of Rortex. Physics of Fluids 2018, 30(11). https://doi.org/10.1063/1.5058939

20. Zhou Z, Li Z, He G. Towards multi-fidelity simulation of flows around an underwater vehicle with appendages and propeller. Theoretical and Applied Mechanics Letters 2022, 12(1), 100318. https://doi.org/10.1016/j.taml.2021.100318

21. Ling X, Leong ZQ, Chin CKH. Free surface effect on the hydrodynamics of an underwater vehicle hullform, the DARPA SUBOFF. International Journal of Maritime Engineering 2022, 164(A1). https://doi.org/10.5750/ijme.v164i1.732

22. Liu S, He G, Wang Z, Luan Z, Zhang Z, Wang W, Gao Y. Resistance and flow field of a submarine in a density stratified fluid. Ocean Engineering 2020, 217, 107934. https://doi.org/10.1016/j.oceaneng.2020.107934

23. Verdoya J, Dellacasagrande M, Barsi. Identification of free-stream and boundary layer correlating events in free-stream turbulence-induced transition. Physics of Fluids 2022, 34(1). https://doi.org/10.1063/5.0079658

24. Qu Y, Wu Q, Zhao X, Huang B, Fu X, Wang G. Numerical investigation of flow structures around the DARPA SUBOFF model. Ocean Engineering 2021, 239, 109866. https://doi.org/10.1016/j.oceaneng.2021.109866

25. Jiménez JM, Hultmark M, Smits AJ. The intermediate wake of a body of revolution at high Reynolds numbers. Journal of Fluid Mechanics 2010, 659, 516-539. https://doi.org/10.1017/S0022112010002715

26. Jiménez JM, Reynolds RT, Smits AJ. The effects of fins on the intermediate wake of a submarine model. Fluids Eng. March 2010, 132(3), 031102. https://doi.org/10.1115/1.4001010

27. Wang S, Shi B, Li Y. A large eddy simulation of flows around an underwater vehicle model using an immersed boundary method. Theoretical and Applied Mechanics Letters 2016, 6(6), 302-305. https://doi.org/10.1016/j.taml.2016.11.004

28. Morse N, Mahesh K. Tripping effects on model-scale studies of flow over the DARPA SUBOFF. Journal of Fluid Mechanics 2023, 975, A3. https://doi.org/10.1017/jfm.2023.777

29. Hartwich CI. Numerical simulation of three-dimensional viscous flow around a submersible body. 1989.

30. Shin MS, Moon IS, Nah YI, Park JC. Measurement of turbulent wake behind a SUBOFF model and derivation of experimental equations. Journal of the Korea Institute of Military Science and Technology 2011, 14(2), 198-204. https://doi.org/10.9766/KIMST.2011.14.2.198

31. Pengwei Z, Xiaoping L, Yuming S. CFD Simulation of the wake turbulence intensity and the dissipation rating of a submarine model. Chinese Journal of Ship Research 2014, 9(3), 43-48. https://doi.org/10.3969/j.issn.1673-3185.2014.03.006

32. Zhang X, Jia S, Zou S, Liu B. A heterogeneous glider system with underwater acoustic communication and positioning. Polish Maritime Research 2024, 31, 154-160. https://doi.org/10.2478/pomr-2024-0045

33. Zieja M, Wawrzyński W, Tomaszewska J. A method for the interpretation of sonar data recorded during autonomous underwater vehicle missions. Polish Maritime Research 2022, 29(3), 176-186. https://doi.org/10.2478/pomr-2022-0038

34. Gunes A. Performance comparison of ToA and TDOA based tracking in underwater multipath environments using Bernoulli filter. Polish Maritime Research 2023, 30(1), 135-144. https://doi.org/10.2478/pomr-2023-0014